Research
Medical Engineering—Article

Pocket Modification of ω-Amine Transaminase *At*ATA for Overcoming the Trade-Off between Activity and Stability Toward 1-Acetonaphthone

Jiaren Cao [a], Fangfang Fan [a], Changjiang Lyu [a], Sheng Hu [b], Weirui Zhao [b], Jiaqi Mei [c], Shuai Qiu [a,*], Lehe Mei [b,d,e,*], Jun Huang [a,*]

[a] *Key Laboratory of Chemical and Biological Processing Technology for Farm Products of Zhejiang Province, Zhejiang Provincial Collaborative Innovation Center of Agricultural Biological Resources Biochemical Manufacturing, School of Biological and Chemical Engineering, Zhejiang University of Science and Technology, Hangzhou 310023, China*
[b] *School of Biological and Chemical Engineering, Ningbo Tech University, Ningbo 315100, China*
[c] *Hangzhou Huadong Medicine Group Co. Ltd., Hangzhou 310011, China*
[d] *College of Chemical and Biological Engineering, Zhejiang University, Hangzhou 310027, China*
[e] *Jinhua Advanced Research Institute, Jinhua 321019, China*

ARTICLE INFO

ABSTRACT

Amine transaminases (ATAs) catalyze the asymmetric amination of prochiral ketones or aldehydes to their corresponding chiral amines. However, the trade-off between activity and stability in enzyme engineering represents a major obstacle to the practical application of ATAs. Overcoming this trade-off is important for developing robustly engineered enzymes and a universal approach for ATAs. Herein, we modified the binding pocket of ω-ATA from *Aspergillus terreus* (*At*ATA) to identify the key amino acid residues controlling the activity and stability of *At*ATA toward 1-acetonaphthone. We discovered a structural switch comprising four key amino acid sites (R128, V149, L182, and L187), as well as the "best" mutant (*At*ATA_D224K/V149A/L182F/L187F; termed M4). Compared to the parent enzyme *At*ATA_D224K (*At*ATA-Pa), M4 increased the catalytic efficiency ($k_{cat}/K_m^{\text{1-acetonaphthone}}$, where k_{cat} is the constant of catalytic activities and is 10.1 min^{-1}, $K_m^{\text{1-acetonaphthone}}$ is Michaelis-Menten constant and is 1.7 mmol·L^{-1}) and half-life ($t_{1/2}$) by 59-fold to 5.9 L·min^{-1}·mmol^{-1} and by 1.6-fold to 46.9 min, respectively. Moreover, using M4 as the biocatalyst, we converted a 20 mmol·L^{-1} aliquot of 1-acetonaphthone in a 50 mL scaled-up system to the desired product, (*R*)-(+)-1(1-naphthyl)ethylamine ((*R*)-NEA), with 78% yield and high enantiomeric purity (*R* > 99.5%) within 10 h. M4 also displayed significantly enhanced activity toward various 1-acetonaphthone analogs. The related structural properties derived by analyzing structure and sequence information of robust ATAs illustrated their enhanced activity and thermostability. Strengthening of intramolecular interactions and expansion of the angle between the substrate-binding pocket and the pyridoxal 5′-phosphate (PLP)-binding pocket contributed to synchronous enhancement of ATA thermostability and activity. Moreover, this pocket engineering strategy successfully transferred enhanced activity and thermostability to three other ATAs, which exhibited 8%–22% sequence similarity with *At*ATA. This research has important implications for overcoming the trade-off between ATA activity and thermostability.

1. Introduction

Chiral amines play essential and wide-ranging roles as the key building blocks of various fine chemicals, agrochemicals [1], bioactive compounds [2], and pharmaceuticals [3]. Approximately 40% of chiral drugs contain chiral amine functional groups [4,5]. (*R*)-(+)-1-(1-naphthyl)ethylamine ((*R*)-NEA) is an extremely important chiral amine used in the synthesis of cinacalcet hydrochloride, a pharmaceutical used to treat secondary hyperthyroidism and hypercalcemia, via amide coupling with 3-(3-trifluoromethylphenyl)-propionic acid [6–8]. (*R*)-NEA is also used as a resolving agent for acid/ester enantiomers because of its weakly basic chemical proper-

ties [9]. Therefore, an efficient and high-atom-economy method for synthesizing (R)-NEA and other chiral amines is urgently required.

Presently, chiral amines are mainly synthesized by traditional chemical methods [10], which require high temperatures, high pressures, protecting groups, and multi-step side procedures [11,12]. In comparison, biocatalytic methods represent powerful alternatives with additional advantages, such as mild reaction conditions; high atom economy; excellent chemo-, regio-, and enantio-selectivity; and sustainability through the application of amine oxidases [13,14], imine reductases [15,16], amine dehydrogenases [17,18], and amine transaminases (ATAs) [19]. For example, Yao et al. [16] synthesized N-substituted α-amino esters via imine reductases with > 99% yield and high enantioselectivity, and Wang et al. [18] used engineered amine dehydrogenases to synthesize (R)-2-amino-4-phenylbutane and 4-(2H-1,3-benzodioxol-5-yl)butan-2-(R)-amine with 85% yield. Among the different biocatalysts in the enzyme library, ω-ATAs can catalyze the asymmetric amination of prochiral ketones or aldehydes to (R)- or (S)-amines with strict stereoselectivity and 100% theoretical yield [20–22], indicating that ω-ATAs are promising biocatalysts for the production of chiral amines.

ATAs (EC 2.6.1.X) are pyridoxal 5′-phosphate (PLP)-dependent enzymes that are divided into fold types I to VII [23]. ω-ATAs belong to the fold-type IV superfamily and are usually homodimers with an active site located at the dimer interface [24]. The active domains of ω-ATAs comprise large and small binding pockets [24]. Although various ω-ATAs exhibit potential performance in the synthesis of chiral amines, their industrial application is still hampered by inherent drawbacks such as unfavorable activity [25], insufficient thermostability [26], poor substrate and organic reagent tolerance [27,28], and unfavorable equilibrium [29], with their low activity and thermostability [30] being particularly limiting for successful bioprocesses.

The trade-off between enzyme activity and stability during enzyme modification represents a particular challenge in current research [31]. Li et al. [32] used a computer-aided design that combined HotSpot Wizard 3.0 and molecular dynamics (MD) simulations to predict hotspot residues and overcome the activity-thermostability trade-off in aldo–keto reductase KmAKR. Cui et al. [33] employed a combined active-site saturation test/iterative saturation mutagenesis strategy to engineer sugar aminotransferases with improved thermostability and activity. Because of the special structural properties of the substrate-binding pockets on the dimer surface of ATAs, the hydrophobicity of the interface and the shape/volume of the pockets have a certain impact on the enzymes [34,35]; thus, various pocket engineering strategies have been developed to enhance activity and thermostability [30,36,37]. Two famous examples in the field of biosynthesis are the production of Sitagliptin by Codexis, Inc. using the engineered ATA-117 obtained by 11 rounds of mutagenesis [38] and the production of the heart failure drug sacubitril precursor ketone acid via engineered (S)-selective ω-ATA [39]. Notably, the different ω-ATAs used in these studies were engineered for only one substrate. Furthermore, studies have typically focused on a single ω-ATA, which makes it difficult to transfer the knowledge gained from one successful robust ω-ATA to another ω-ATA desired for its diverse amino acid sequences and different targeting substrates. Therefore, it is important to develop general sequential structural methods and clarify the related mechanisms to overcome the trade-off between activity and thermostability toward prochiral ketones/aldehydes such as 1-acetonaphthone.

This study aimed to overcome the activity–stability trade-off of ω-ATA from Aspergillus terreus (AtATA) toward 1-acetonaphthone by engineering the binding pockets. Specifically, we clone a gene encoding 325 amino acids of AtATA and express this gene in Escherichia coli (E. coli) [40]. Wild-type AtATA (AtATA_WT) exhibits low activity and poor stability, with a half-life ($t_{1/2}$) of 6.9 min at 40 °C [41]. Therefore, we establish a semi-rational strategy involving charge–charge interactions to improve AtATA thermostability without sacrificing activity. The $t_{1/2}$ of mutant AtATA_D224K (designated as AtATA-Pa) is 29.2 min [42]; using AtATA-Pa as a template, we identify the key residues that control activity and stability. We then construct a structural switch comprising these key amino acids and summarize the related structural properties to validate and analyze ATAs with available structures through structural and sequential information of their activity and stability. We then successfully transfer the strategy that enhanced activity-stability achieved in AtATA via pocket engineering to three other ATAs that exhibit 8%–22% sequence similarity with AtATA. Furthermore, we use the "best" mutant AtATA_D224K/V149A/L182F/L187F (designated as M4) as a biocatalyst to convert 20 mmol·L^{-1} 1-acetonaphthone to the desired product ((R)-NEA) with 78% yield and high enantiomeric purity (R > 99.5%) within 10 h.

2. Materials and methods

2.1. Chemicals, bacterial strains, and plasmids

AtATA complementary DNA (cDNA), including the NcoI and XhoI restriction sites, was synthesized by General Biosystems, Inc. (China), and the plasmid pET-28a(+) was used for gene cloning. The parent variant AtATA-Pa with improved thermostability was obtained previously by the charge–charge interaction strategy and stored in our lab [39]. All polymerase chain reaction (PCR) primers were synthesized by Beijing Tsingke Biotech Co., Ltd. (China) and listed in Table S1 in Appendix A. Unless otherwise stated, all other reagents and chemicals were of analytical grade and purchased from J&K Chemical Ltd. (China) and Sigma-Aldrich (China) without further purification.

2.2. Colorimetric screening method

A two-step screening approach was used to screen for mutants with high activity and thermostability, as previously described [43]. The assay was performed in a colonies reaction containing 25 mmol·L^{-1} 2-(4-nitrophenyl)ethan-1-amine hydrochloride, 10 mmol·L^{-1} 1-acetonaphthone, 0.1 mmol·L^{-1} PLP, 20% (v/v) dimethyl sulfoxide (DMSO), and 50 mmol·L^{-1} phosphate-buffered saline (PBS, pH 8.0, Fig. S1 in Appendix A). A hybond-N membrane with colonies covering the filter paper was pre-soaked with the pre-screening solution, and the reaction was incubated at 30 °C for 1 h. Controls were also performed; one without adding the amine acceptor and another without adding the enzyme. Orange/red coloration indicated that AtATAs were active toward 1-acetonaphthone (Figs. S2–S4 in Appendix A).

Colonies with the deepest reddish-brown color on each membrane were selected and expressed 8 h in 96 deep wells with equal concentrations of isopropylthio-β-galactoside (IPTG). After incubation, the cells were collected by centrifugation for 15 min (6000 revolutions per minute (rpm), 4 °C) and washed twice with PBS (50 mmol·L^{-1}, pH 8.0). Detection was achieved in a total volume of 200 μL containing 50 μL of the cell diluent and 150 μL of the reaction solution. The reaction was incubated at 30 °C and 500 rpm for 30 min, and the optical density difference at 450 nm (ΔOD_{450}) value was used to examine the rates (Fig. S5 in Appendix A). The standard curve of (R)-NEA was verified using high-performance liquid chromatography (HPLC) (Fig. S6 in Appendix A).

2.3. Mutagenesis and screening

All variants were prepared using a modified version of the QuikChange® PCR method using pET-28a(+)-AtATA_D224K as the

template. For each reaction, 12.5 μL of DNA polymerase mix, 2 μL of parental plasmid, and 1 μL of each primer were diluted to 25 μL with double distilled H$_2$O (ddH$_2$O). The amplification was performed as follows: ① 95 °C, 3 min; ② 35 cycles: 95 °C, 20 s; 55 °C, 20 s; 72 °C, 1.5 min; ③ 72 °C, 7 min. The remaining non-methylated purified DNA was transformed into *E. coli* BL21(DE3) competent cells after digestion by Dpn I (20 units of enzyme activity (U)) at 37 °C for 2 h.

2.4. Protein expression and purification

Preserved *E. coli* BL21(DE3)/pET-28a(+)-*At*ATA-Pa and *E. coli* BL21(DE3)/pET-28a(+)-*At*ATA-mutants were inoculated in Luria-Bertani (LB) medium (200 mL) containing 50 μg·mL^{-1} kanamycin at 37 °C for 3 h until optical density at 600 nm (OD$_{600}$) reached approximately 0.6. Enzyme expression was induced by 200 μg·mL^{-1} IPTG at 25 °C and 150 rpm for 20 h. The cells were harvested, centrifuged for 10 min at 8000 rpm at 4 °C, and dissolved in binding buffer (20 mmol·L^{-1} imidazole, 50 mmol·L^{-1} PBS, pH 8.0) for high-pressure homogenization. The cleared lysate was obtained by centrifugation at 8000 rpm and 4 °C for 10 min, then microfiltered through 0.45-μm membranes. Enzymes with histidine 6 (His6)-tag were purified using nickel-affinity chromatography and eluted with 250 mmol·L^{-1} imidazole in 50 mmol·L^{-1} PBS (pH 8.0). Protein expression and purification were analyzed by sodium dodecyl sulfate-polyacrylamide gel electrophoresis (SDS-PAGE).

2.5. Activity assay

To measure the activities of the ATA variants, the reaction was performed in a 500 μL volume with 50 mmol·L^{-1} PBS (pH 8.0) containing 0.05–0.50 g·L^{-1} purified *At*ATAs, 10 mmol·L^{-1} 1-acetonaphthone, 10 mmol·L^{-1} 1-(*R*)-phenylethylamine (1-(*R*)-PEA), 20% (v/v) DMSO, and 0.1 mmol·L^{-1} PLP. The reaction mixture was shaken at 30 °C and 500 rpm for 30 min. An aliquot of the mixture (100 μL) was diluted with 50% acetonitrile and analyzed by HPLC. One U was defined as the amount of enzyme required to form 1 μmol of (*R*)-NEA per minute under optimum conditions. The specific activity was expressed as units of activity per gram of purified enzyme (U·g^{-1}). All experiments were conducted in triplicate.

2.6. Determination of kinetic parameters and thermostability

The kinetic parameters were estimated by measuring the initial velocities of the enzyme reaction and curve fitting according to the Michaelis-Menten equation. For the kinetic characterization of purified *At*ATA-Pa and its variants to 1-acetonaphthone, an activity assay was performed in a mixture containing various concentrations of 1-acetonaphthone (1–15 mmol·L^{-1}) using 10 mmol·L^{-1} 1-(*R*)-PEA. For 1-(*R*)-PEA, 1-acetonaphthone (10 mmol·L^{-1}) and 1-(*R*)-PEA (1–15 mmol·L^{-1}) were used for the enzyme kinetic assay. For half-inactivation temperature (T_{50}^{10}) measurements, *At*ATAs were incubated at different temperatures (10–60 °C) for 10 min, then swiftly cooled in an ice bath for 5 min. The activities of *At*ATAs were detected at 30 °C and pH 8.0, where the original activity was designated as 100%. All assays were performed in triplicates. The $t_{1/2}$ of purified *At*ATAs were determined by incubating each purified protein (1.0 g·L^{-1}) at 40 °C for an appropriate time of 10–60 min, followed by measurement of the residual activity. The $t_{1/2}$ values were calculated according to the first-order deactivation functions, $\ln(A/A_0) = -k_d t$ and $t_{1/2} = \ln2/k_d$, where A_0 is the initial activity, A is the residual activity at time t during thermal deactivation, and k_d is the deactivation rate constant (h^{-1}). The melting temperatures (T_m) of *At*ATAs were determined using differential

scanning fluorimetry (DSF) [44]. Aliquots of each mixture (50 μL) in final concentrations of 1 μL 1× SYPRO Ruby orange dye (dissolved in DMSO) and 0.1 g·L^{-1} *At*ATAs were diluted with buffer (150 mmol·L^{-1} NaCl, 50 mmol·L^{-1} PBS, pH 8.0) and pre-incubated at 4 °C for 20 min. The DSF protocol involved an initial temperature of 20 °C, after which the temperature was increased to 75 °C at a rate of 1.4 °C·min^{-1}. Fluorescence was measured using real-time PCR, and the data was collected in increments of 0.7 °C. The excitation and emission wavelengths were 490 and 605 nm, respectively. All experiments were conducted in triplicate. The T_m was calculated using the formula shown in Eq. (1):

$$y = UF + \frac{NF - UF}{1 + e^{\frac{T_m - x}{\alpha}}} \tag{1}$$

where UF and NF are the minimum and maximum emission fluorescence intensities, respectively; α is the slope of the curve within T_m; x, y, and e represent the set temperature, fluorescence intensity, and natural constant, respectively.

2.7. Biocatalytic synthesis of (R)-NEA

The biocatalytic synthesis of (*R*)-NEA by *At*ATAs was performed using a 50 mL scaled-up system. The reaction conditions were as follows: 20 mmol·L^{-1} 1-acetonaphthone with 20 mmol·L^{-1} 1-(*R*)-PEA (or 30 mmol·L^{-1} 1-acetonaphthone with 30 mmol·L^{-1} 1-(*R*)-PEA), 50 mmol·L^{-1} PBS (pH 8.0), 20% (v/v) DMSO, 0.1 mmol·L^{-1} PLP, and 1.0 g$_{DCW}$·L^{-1} (DCW: dry cell weight) *At*ATAs by *E. coli* expression. The sealed reaction vial was incubated in a thermal shaker at 30 °C and 800 rpm. After 25 h, the samples were diluted and analyzed by HPLC.

2.8. Substrate specificity

A substrate specificity assay was performed to measure the activity of *At*ATAs toward various aromatic ketones, referring to the methods detailed above (Sections 2.5 and 2.7). The substrate spectrum contained data on enzyme activity and stereoselectivity for different substrates.

2.9. Molecular docking and MD simulation

The crystal structure of *At*ATA was resolved (Protein Data Bank (PDB) ID: 4CE5) and used as the initial model for constructing mutant models [40]. Based on this model, mutant models were built by energy minimization after mutation at the corresponding site using YASARA (version 16.4.6) software†. Docking studies were performed using the Discovery Studio 2019 Client. Molecular modeling of *At*ATA (PDB ID: 4CE5), with 1-acetonaphthone as the ligand, was performed using the CHARMm force field on CDOCKER under default settings within the active site defined by the binding-site module. We selected the most stable docking pose showing the spatial orientation of the substrate and performed stepwise chemical modifications to generate an external aldimine and quinonoid structure.

MD simulations were performed in a constant system (313 K, pH 8.0) for 50 ns using the Amber14 force field of YASARA (version 16.4.6) [45]. A stable structure was acquired using a transferable interatomic potential with three points (TIP3P) water model filled with Na$^+$ and Cl$^-$ (0.9%) to neutralize the total net charge of the systems.

For visualization of the active site, PDB structures were loaded into PyMOL (version 2.0.7) and Discovery Studio 2019 Client. The active site charge was calculated using the APBS Electrostatics

---

Plugin for PyMOL and visualized accordingly. PyMOL and visual molecular dynamics (VMD) (version 1.9) were used for visualization and analysis [46]. The homologs and variants are available in the RCSB database† and were optimized using the BuildModel module of FoldX‡.

2.10. Mutation site grafting

To verify whether the mutation site was consistent with our expectations, we transplanted it into three other ATAs with different structures to observe its catalytic activity toward 1-acetonaphthone. According to structure and sequence alignment, these four sites corresponded to R128, V149, L182, and L187 of the alternative ATAs. ATAs' activities were determined according to the following reaction system (1 mL), which contained 0.25 g·L^{-1} purified enzyme solution, 10 mmol·L^{-1} 1-acetonaphthone, 10 mmol·L^{-1} different amino donor (L-leucine, 1-(R)-phenethylamine, or 1-(S)-phenethylamine), and 0.1 mmol·L^{-1} PLP, 20% (v/v) DMSO. The reaction was performed at the optimum temperature and pH, and the product was analyzed as described above.

3. Results and discussion

3.1. Identification of potential residues by structural analysis

As reported previously, AtATA (PDB ID: 4CE5) is a homodimer with large and small substrate-binding pockets located at the dimer interface [23]. Many findings suggest that the multimeric interfaces of enzymes are essential for their activity and thermostability because the interfaces are more hydrophobic and form inter-H-bonds and hydrophobic interactions between subunits, which affect the overall function of the protein complex [47]. Therefore, redesigning or reshaping the substrate-binding pocket to regulate steric constraints and the microenvironment can be particularly effective for enhancing the catalytic activity and thermostability of AtATAs. AtATA-catalyzed asymmetric ammoniation follows the ping-pong bi-bi mechanism in two steps. Initially, PLP is covalently bound as a Schiff base to the ε-group of the active site, lysine (K). In the first step, the amine groups of 1-(R)-PEA (amino donor, obtained through screening as shown in Table S2 in Appendix A) are transported to PLP while the PLP is converted to pyridoxamine-5′-phosphate (PMP); the second step is the transfer of amine groups from PMP to 1-acetonaphthone (amino acceptor) to generate a chiral amine and regenerate PLP. Given the volume of 1-(R)-PEA and 1-acetonaphthone carrying a naphthalene ring (containing ten carbons), accommodation of the substrate-binding pocket limits the catalytic activity of AtATA. As shown in Figs. 1(a) and (b), the amino acceptor 1-acetonaphthone was docked into the substrate-binding pocket of the AtATA–PLP complex and generated a pro-R ligand-binding conformation with binding energy of –26.32 kcal·mol^{-1}.

To alleviate steric hindrance and redesign substrate-enzyme interactions, 11 pocket-decorating sites, including three residues (R128, V149, and V147) at the entrance of the binding pocket (Fig. 1(c)) and eight residues (Y60, V62, L182, W184, L187, V238, A276, and L235) at the binding pocket (Fig. 1(d)), were selected as potentially beneficial residues because the key residues for enhancing activity and thermostability were usually located either in the binding pocket or close to the pocket of the dimer interface. NNK (N = A/T/C/G, K = G/T) degeneracy codons encoding 20 amino acids with various characteristic side chains were used for library

construction. Subsequently, 220 potential variants were generated and confirmed using gene sequencing. The protein mutability landscape is shown in Fig. 1(e). Among them, 22 variants at four sites showed improved residual activity toward 1-acetonaphthone, whereas others showed decreased or inactive variants. We identified four single mutants at four sites on the dimer interface (Fig. 1(f)), V149A, L182F, L187F, and R128L, taking AtATA-Pa as a template that displayed excellent residual activity among the 11 sites. Furthermore, four single mutants were rescreened, the specific activity and enantiomeric excess (*e.e.*) values were assayed, and a combination of single mutants was subsequently applied to enhance the activity. As shown in Table 1, all double, triple, and quadruple mutants exhibited higher specific activities than the four single mutants did. Meanwhile, the mutant M4 showed the highest improved activity, with 22.2-fold higher relative activity than AtATA-Pa; this "best" mutant was set as the research object in subsequent analyses

3.2. Measurement of kinetic and thermodynamic parameters and (R)-NEA production

The thermostabilities (Table 2) and kinetic parameters (Table 3) of AtATA-Pa and M4 were characterized. The Michaelis-Menten constant of M4 for 1-acetonaphthone $K_m^{\text{1-acetonaphthone}}$ decreased to 1.7 mmol·L^{-1}, whereas that for 1-(R)-PEA increased to 1.2 mmol·L^{-1}. The catalytic efficiency (k_{cat}/K_m; k_{cat}: the constant of catalytic activities) of M4 for 1-acetonaphthone and 1-(R)-PEA increased to 5.9 and 7.8 L·min^{-1}·mmol^{-1}, respectively, which were 58.0 and 1.2-fold higher than those of AtATA-Pa. Thermostability was assessed by measuring T_{50}^{10}, $t_{1/2}$ (40 °C), and T_m values. The T_{50}^{10}, $t_{1/2}$, and T_m values for M4 increased to 46.5 °C, 46.9 min, and 48.4 °C, respectively, indicating an increase of 2.0 °C, 1.6-times, and 0.8 °C from those for AtATA-Pa. Trade-off between activity and thermostability was not observed, and synchronous enhancement was achieved. Furthermore, the asymmetric synthesis of (R)-NEA was conducted in a 50 mL scaled-up system using M4 as the biocatalyst. The 20 mmol·L^{-1} substrate 1-acetonaphthone was converted into (R)-NEA (yield > 75%, *e.e.*: R > 99.5%) within 10 h using only 1 g·L^{-1} of lyophilized *E. coli* expressing M4. When the substrate concentration was gradually increased from 20 to 30 mmol·L^{-1}, the conversion of 30 mmol·L^{-1} 1-acetonaphthone reached almost 50% within 12 h. In summary, M4 exhibited better catalytic performance than AtATA-Pa in a 50 mL scaled-up system (Fig. 2). Compared to other engineered ATAs acquired using different strategies, M4 exhibited excellent catalytic efficiency and performance (Tables S3 and S4 in Appendix A).

3.3. Structural basis of AtATAs with enhanced activity and thermostability

To generate a molecular basis for the structural changes and enzyme activity, we analyzed the substrate-binding pockets and interactions of various mutants of AtATA with different activities. As shown in Fig. S7 in Appendix A, the volumes of the large and small substrate-binding pockets did not change significantly with evolution of AtATA-Pa (1132.9 Å^3) to the "best" mutant M4 (1139.5 Å^3). However, the relative positional relationship between the substrate-binding pocket and PLP-binding pocket differed after the mutation, which was attributed to the catalytic efficiency. The initiation of amination is mediated by increased electrophilicity of the carbonyl group of the acceptor and is activated by the H bond between O (amino acceptor) and NH$_3^+$ (K180); subsequently, the amino acceptor is attacked by a nucleophile from PMP [22]. Hence, we proposed a characteristic angle (θ, $\angle C_{\alpha\text{-amino acceptor}} - C_{\alpha\text{-PMP}} - C_{\beta\text{-PMP}}$) constructed by $C_{\alpha\text{-amino acceptor}} - C_{\alpha\text{-PMP}}$ and $C_{\alpha\text{-PMP}} - C_{\beta\text{-PMP}}$, and a distance ($D_{\text{C-N}}$) between $C_{\alpha\text{-amino acceptor}}$ of the amino

---

† https://www1.rcsb.org/.
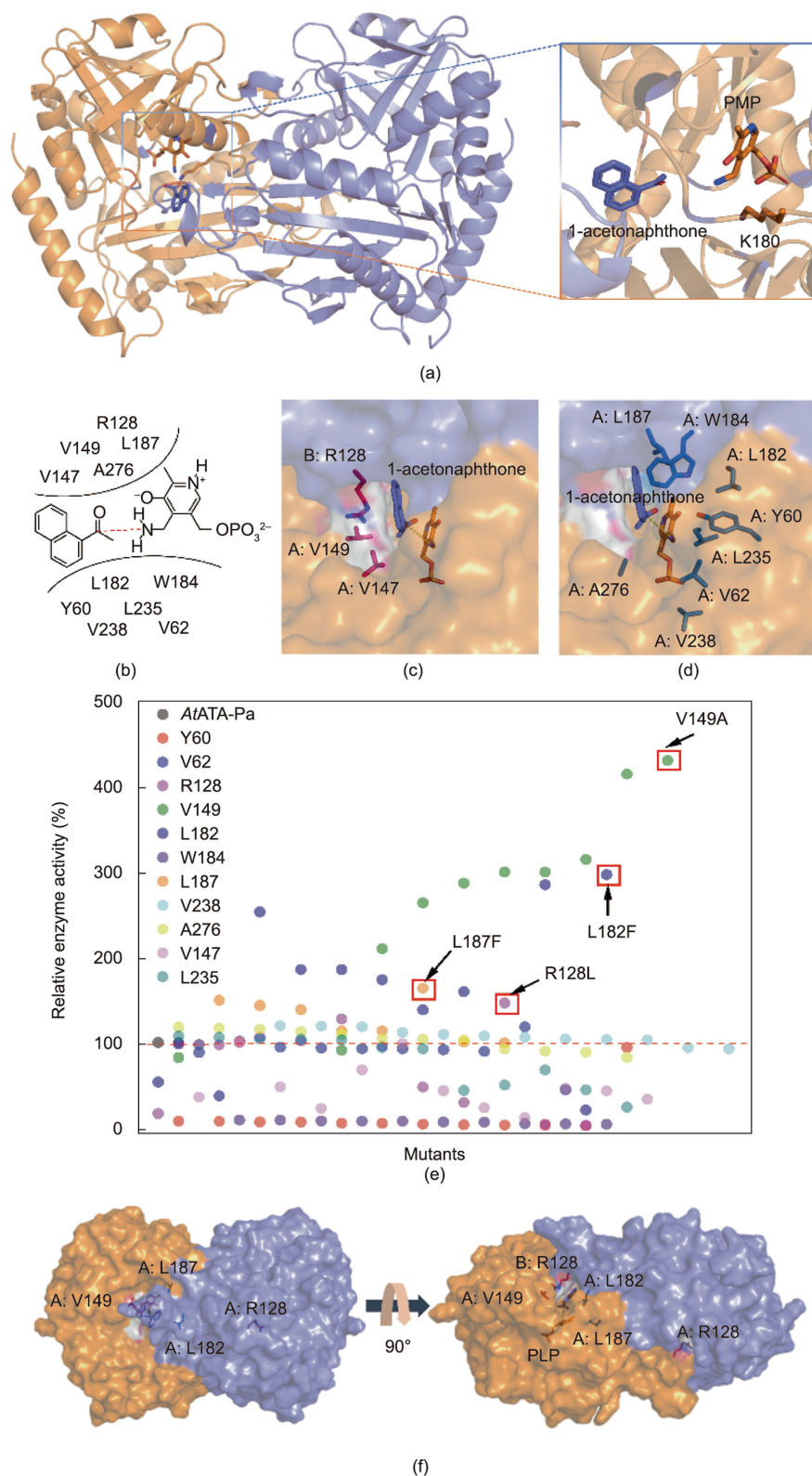
‡ https://foldxsuite.crg.eu.

Fig. 1. Structural insights into the 3-D model of *At*ATA. (a) Cartoon drawing with PLP modeled in. (b) Close-up view of the catalytic site geometry. (c) The magnified view of residues at the entrance of the substrate-binding pocket. (d) The magnified view of residues within the substrate-binding pocket. PLP and 1-acetonaphthone are illustrated as orange and purple sticks. The residues are marked as red and blue sticks. (e) The effect of each single mutant on *At*ATA-Pa relative activity. (f) The distribution of mutation sites. All the mutants were incubated for 30 min at 40 °C to measure the residual activity. The residual activity of *At*ATA-Pa was defined as 100%.

acceptor and N of –NH₂ in PMP (red and blue lines in Fig. 3(a), respectively). As shown in Fig. 3(b), the angle presented between the substrate- and PLP-binding pocket (θ_{pocket}) matches the angle constructed by $C_{\alpha\text{-amino acceptor}}$–$C_{\alpha\text{-PMP}}$ and $C_{\alpha\text{-PMP}}$–$C_{\beta\text{-PMP}}$. The angle presented between the substrate- and PLP-binding pockets changed from an acute angle in *At*ATA-Pa ($\theta_0 = 82.9°$) to an obtuse angle

Table 1
The enzyme activity toward 1-acetonaphthone and stereoselectivity of *At*ATA-Pa and its variants.

Enzymes	Specific activity (U·g⁻¹)[a]	Relative activity[a]	*e.e.*
*At*ATA-Pa	10.9 ± 0.2	100.0%	R > 99.5%
V149A	47.2 ± 0.7	433.0% ± 5.9%	R > 99.5%
R128L	16.0 ± 1.9	146.8% ± 9.8%	R > 99.5%
L182F	32.5 ± 0.8	298.2% ± 7.7%	R > 99.5%
L187F	17.9 ± 0.1	164.2% ± 3.5%	R > 99.5%
V149A/R128L	121.5 ± 1.6	1114.7% ± 15.5%	R > 99.5%
L182F/L187F	133.1 ± 1.7	1221.1% ± 20.3%	R > 99.5%
V149A/L182F	197.9 ± 2.3	1815.6% ± 16.6%	R > 99.5%
V149A/L187F	50.7 ± 0.8	465.1% ± 10.2%	R > 99.5%
R128L/L182F	104.5 ± 2.5	958.7% ± 22.3%	R > 99.5%
R128L/L187F	112.9 ± 1.4	1035.8% ± 19.9%	R > 99.5%
M4	242.4 ± 2.6	2223.9% ± 28.6%	R > 99.5%
R128L/V149A/L187F	208.1 ± 2.2	1909.2% ± 18.7%	R > 99.5%
R128L/V149A/L182F	135.8 ± 1.2	1245.9% ± 11.9%	R > 99.5%
R128L/V149A/L182F/ L187F	207.1 ± 2.9	1900.0% ± 30.7%	R > 99.5%

[a] Reaction condition: 10 mmol·L⁻¹ 1-acetonaphthone, 10 mmol·L⁻¹ 1-(*R*)-PEA, 20% (v/v) DMSO, 0.1 mmol·L⁻¹ PLP, and 0.05–0.50 g·L⁻¹ purified enzyme in PBS (50 mmol·L⁻¹, pH 8.0) at 30 °C. Experiments were conducted in triplicate.

in M4 (θ_7 = 104.7°). Furthermore, single, double, triple, and quadruple mutants, which exhibited various activities, were selected to analyze changes in the angles between the substrate- and PLP-binding pockets. The relative position of PMP and the amino acceptor showed a leverage structure, resulting in an obtuse angle structure that would bring the –NH₂ of PMP closer to the amino acceptor and reduce D_{C-N} (Fig. 3(c)). Furthermore, As the activity increased, the angles between the substrate- and PLP-binding pockets tended to increase (Fig. 4) from *At*ATA-Pa (θ_0) to the various mutants ($\theta_1-\theta_6$). We speculated that the enhanced activities were related to the angles between the substrate- and PLP-binding pockets as they could accommodate bulkier substrates.

Based on the above theoretical inference, we investigated the binding pocket structures of six reported ATAs with available structures and high catalytic activity toward bulky ketones to obtain a more universal theoretical basis (Fig. S8 in Appendix A).

The overall structures of these six enzymes comprise a substrate-binding domain, a catalytic site, and a PLP-binding domain, in which three enzymes (PDB IDs: 3WWJ, 1KT8, and 3DAA) belong to (*R*)-ATA and three enzymes (PDB IDs: 3GJU, 3HMU, and 3I5T) belong to (*S*)-ATA. The structural differences between (*R*)-ATA and (*S*)-ATA endow them with diverse functional properties and enable the generation of (*R*)- or (*S*)-selective chiral amines. The angles between the substrate- and PLP-binding pockets of all six (*R*)- or (*S*)-ATAs were 90°–180°. This result implied that an obtuse angle between the substrate- and PLP-binding pockets is a prerequisite for obtaining high-activity ATAs.

To test our proposed hypothesis and identify the key positions that control the angle of the substrate- and PLP-binding pockets, multiple sequence alignment was performed (Fig. S9 in Appendix A). Seventeen reported ATAs were mined from the NCBI database for multiple sequence alignment. These ATAs display approximately 60%–85% amino acid sequence identity with *At*ATA. All 18 ATAs (including *At*ATA) contain a conserved catalytic site (K). The R/L residue was conserved at positions 128/182 (Fig. S9(a)). Positions 149 and 187 were non-conserved and displayed the sequence differences. That is, two of the 18 ATAs had A at position 149 (residue number of *At*ATA) and two of the 18 ATAs had P at position 187 (the residue number of *At*ATA), whereas 16 out of 18 had L in this position. These results indicate that sequences from different sources showed a high sequence consensus. In the phylogenetic tree, *At*ATA showed high amino acid sequence identity with ATAs from *Aspergillus terreus* (> 90%) and moderate identity with ATAs from *Diaporthe* and *Pseudogymnoascus* (Fig. S9(b)). Eight ATAs with available structures (including (*R*)- and (*S*)-ATAs) were mined from the PDB and aligned with *At*ATA. Subsequently, we verified four key residues (R128, V149, L182, and L187) that influenced the angles between the substrate- and PLP-binding pockets using structural analysis (Fig. S9(c) and Table S5 in Appendix A). Four key positions were located at or close to the binding pocket, and multiple sequence alignments of the sequences showed that these four positions were not conserved and exhibited residue diversification. K located at positions L182F and L187F was substituted with a bulky F to broaden the angle between the substrate- and PLP-binding pockets. Small residues are preferred at position 149, and all four residues prefer hydrophobic amino acids. The hydrophilicity/hydrophobicity of *At*ATA-Pa and M4 were not significantly different (Fig. S10 in Appendix A).

Static (docking and modeling) and dynamic analyses (MD simulations) of *At*ATA structures were performed to investigate how the substitutions enhanced the activity and thermostability of 1-acetonaphthone. After MD simulation of the protein–ligand
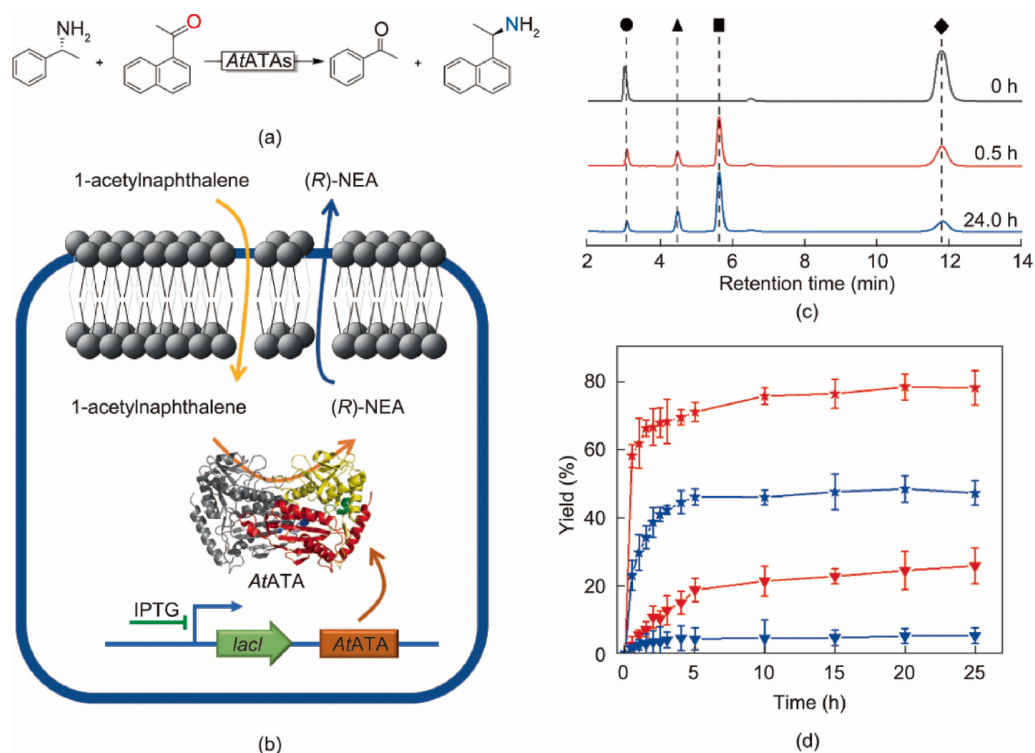
Table 2
The thermostabilities of *At*ATA-Pa and M4.

Enzyme	$t_{1/2}$ (min)	k_d (h⁻¹)	T_m (°C)	ΔT_m (°C)	T_{50}^{10} (°C)	ΔT_{50}^{10} (°C)
*At*ATA-Pa	29.2 ± 0.2	1.4	47.6 ± 0.1	—	44.5 ± 0.2	—
M4	46.9 ± 0.4	0.9	48.4 ± 0.3	0.8	46.5 ± 0.5	2.0

ΔT_m: the difference between M4 and *At*ATA-Pa on T_m; ΔT_{50}^{10}: the difference between M4 and *At*ATA-Pa on T_{50}^{10}.

Table 3
The kinetic parameters[a] of *At*ATA-Pa and M4 toward 1-acetonaphthone or 1-(*R*)-PEA.

Enzymes	$k_{cat}^{1-(R)-PEA}$ (min⁻¹)	$K_m^{1-(R)-PEA}$ (mmol·L⁻¹)	$k_{cat}/K_m^{1-(R)-PEA}$ (L·min⁻¹·mmol⁻¹)	Fold[b]	$k_{cat}^{1-acetonaphthone}$ (min⁻¹)	$K_m^{1-acetonaphthone}$ (mmol·L⁻¹)	$k_{cat}/K_m^{1-acetonaphthone}$ (L·min⁻¹·mmol⁻¹)	Fold[c]
*At*ATA-Pa	0.7 ± 0.1	0.2 ± 0.1	3.5	1.0	0.7 ± 0.1	8.2 ± 0.2	0.1	1.0
M4	9.4 ± 0.2	1.2 ± 0.1	7.8	2.2	10.1 ± 0.2	1.7 ± 0.1	5.9	59.0

[a] Kinetic parameters were determined at pH 8.0 and 30 °C using purified enzymes.
[b] Fold of improvement in k_{cat}/K_m over the *At*ATA-Pa enzyme toward 1-(*R*)-PEA.
[c] Fold of improvement in k_{cat}/K_m over the *At*ATA-Pa enzyme toward 1-acetonaphthone.

Fig. 2. The biosynthesis of (*R*)-NEA catalyzed by *At*ATAs. (a) Chemical reaction formula of asymmetric synthesis of (*R*)-NEA from 1-acetonaphthone by *At*ATAs. (b) Shematic illustration of *E. coli* cells expressing *At*ATAs for synthesizing (*R*)-NEA from 1-acetonaphthone. *LacI*: the regulator gene encoding repressor in lactose operon. (c) HPLC analysis of the conversion of 1-acetonaphthone by M4. The retention times of (●) 1-(*R*)-PEA, (▲) acetophenone, (◆) 1-acetonaphthone, and (■) the product (*R*)-NEA were 3.1, 4.4, 11.8, and 5.7 min, respectively. Reaction mixture contained 1.0 $g_{DCW}·L^{-1}$ *E. coli* expressing M4, 20 $mmol·L^{-1}$ 1-(*R*)-PEA, 20% (v/v) DMSO, and 0.1 $mmol·L^{-1}$ PLP in PBS (50 $mmol·L^{-1}$, pH 8.0). (d) Time course of asymmetric synthesis of (*R*)-NEA from 1-acetonaphthone by (▼) *At*ATA-Pa and (★) M4. Substrate concentrations were 20 (red) and 30 (blue) $mmol·L^{-1}$, respectively. Reaction mixture contained 1.0 $g_{DCW}·L^{-1}$ *E. coli* expressing *At*ATAs, 20–30 $mmol·L^{-1}$ 1-(*R*)-PEA, 20% (v/v) DMSO, and 0.1 $mmol·L^{-1}$ PLP in PBS (50 $mmol·L^{-1}$, pH 8.0). The reaction was shaken at 30 °C, 500 rpm in a 50 mL scale-up.
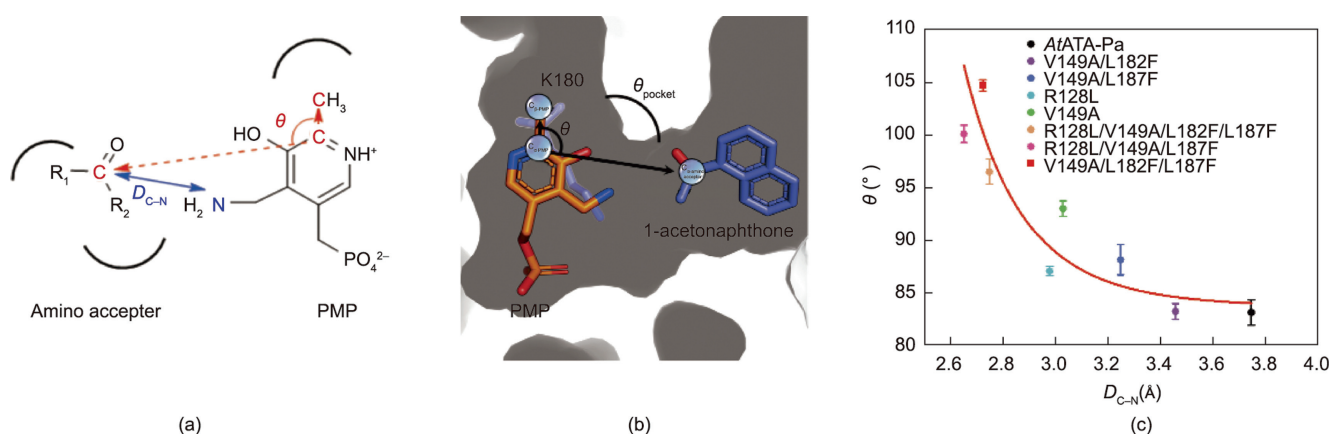

Fig. 3. Correlation between θ ($\angle C_{\alpha\text{-amino acceptor}}$–$C_{\alpha\text{-PMP}}$–$C_{\beta\text{-PMP}}$) and $D_{C–N}$. (a) Graphical representation of θ and $D_{C–N}$. (b) The three-dimensional spatial location of θ ($\angle C_{\alpha\text{-amino acceptor}}$–$C_{\alpha\text{-PMP}}$–$C_{\beta\text{-PMP}}$) and the angle between the substrate- and PLP-binding pocket θ_{pocket}. (c) Nonlinear relationship between θ and $D_{C–N}$ via docking analysis. The red square and black circle represent the docking results of M4 and *At*ATA-Pa.

complex with a relatively stable structure (Fig. S11 in Appendix A), the substrate-binding pocket displayed increased π–π interaction (Figs. 5(a) and (b)) when V149, L182, and L187 were substituted by A, F, and F, respectively. Obviously, the phenyl ring in the phenylalanine at positions L182F and L187F enhanced the π–π interactions between residues and the surrounding amino acids. This was beneficial for improving enzyme thermostability. In addition, the substrate 1-acetonaphthone was docked into *At*ATA-Pa or

M4, and the form of π–π interaction between T stacking (offset face-to-face) or F stacking (edge-to-face) showed an increasing trend from *At*ATA-Pa to M4 (Figs. 5(c)–(f)). Moreover, compared to *At*ATA-Pa, M4 exhibited a shortened reaction distance (H-bond distance or nucleophilic attack distance) between the ε-amino hydrogen of K and the carbonyl oxygen of 1-acetonaphthone, as well as between the amino nitrogen of PMP and the carbonyl carbon of 1-acetonaphthone, and the binding energy was decreased
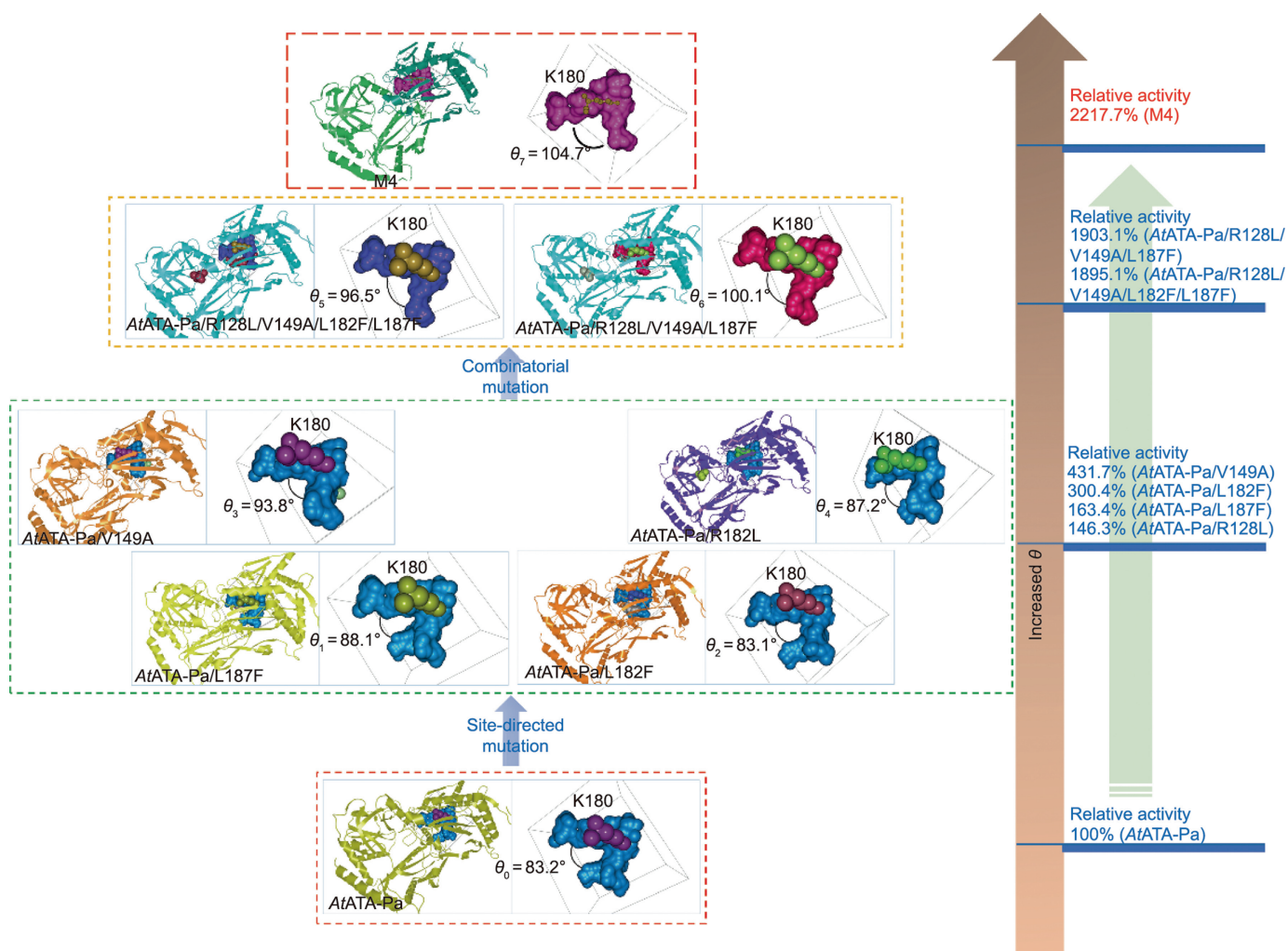
Fig. 4. The landscape of the θ change between substrate- and PLP-binding pockets of different mutants. The stable state structure of the protein after energy minimization was used for docking analysis.

(Figs. 5(c) and (d)). These results were consistent with the enhanced affinity of the "best" mutant enzyme M4 to 1-acetonaphthone.

As shown in Fig. S12 in Appendix A, four loops (loop A: 146–150, loop B: 164–183, loop C: 231–236, and loop D: 267–277) surround the substrate-binding pocket of *At*ATAs, and structural changes in these binding-pocket loops can affect enzyme stability. The introduction of L182F and L187F decreased the flexibility of loop C and loop D because of increased π–π interactions (Table S6 in Appendix A). The hydrogen bonds and hydrophobic interactions did not change significantly from *At*ATA-Pa to M4, and the added-anion interaction was an essential factor for improving thermostability. Following analysis of the interactions between or within molecules of *At*ATA or M4 via Discovery Studio 2019 Client, we counted the number of H-bonds and electrostatic, hydrophobic, and salt bridges. Because *At*ATA is present as a dimer and the substrate-binding pocket is located at the dimer interface, the substitution of local amino acids will influence the interaction between or within monomers. The total number of interactions between monomers decreased and the number of interactions within monomers increased from *At*ATA-Pa to M4 (Fig. S13 in Appendix A). This suggests that a loose state existed between the monomers after mutation, and that the interior of the monomer was more compact. Thus, the substrates entered the binding

pocket more easily, resulting in a more stable overall structure of M4.

3.4. Analysis of amine transaminase grafting

As mentioned above, an approach was developed based on sequence–structure–function analysis and pocket engineering to predict ATAs with the desired asymmetric ammoniation toward 1-acetonaphthone and to guide the semi-rational design for engineering the co-evolution of activity and stability. Following this approach, we analyzed three potential ATA-coding sequences (amino acid length of 280–360; Fig. S14 in Appendix A) using *At*ATA as a template (8%–22% sequence similarity). *BC*AT [48] and *Pd*ATA [27] belong to (*S*)-selective ATA, whereas ATA-117-Rd11 belongs to (*R*)-selective ATA [38]. Furthermore, ATA-117-Rd11 and *Pd*ATA are prone to catalyze aromatic ketones, whereas *BC*AT preferentially catalyzes aliphatic ketones. Therefore, the selected ATAs with different chiral selectivities and substrate scopes were more representative for identifying key amino acid sites acquired via the pocket engineering strategy. The activities and thermostabilities of these three ATAs were modified by characterizing their substrate- and PLP-binding pockets and their intramolecular interactions. To verify the key structural switch, three ATA genes were synthesized and expressed in *E. coli*, and their activity and
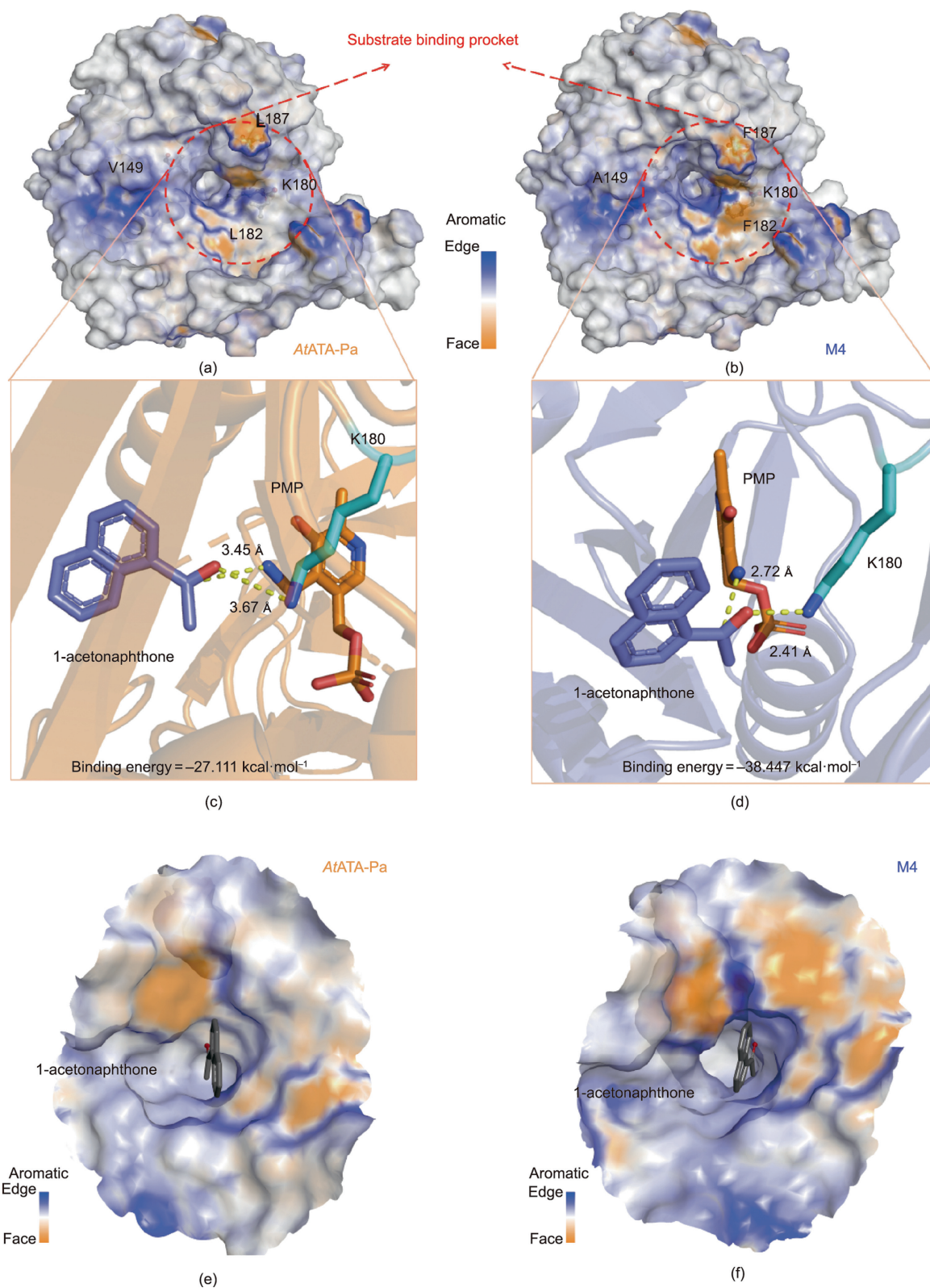
Fig. 5. π–π interactions within the monomeric molecules of (a) *At*ATA-Pa or (b) M4. Orange: offset face-to-face, T stacking; Blue: edge-to-face, F stacking. Binding orientations of the substrate 1-acetonaphthone and PLP in the active site of (c) *At*ATA-Pa by docking or (d) M4. Docking was performed with YASARA. π–π interactions between the monomeric molecules of (e) *At*ATA-Pa or (f) M4 and ligand 1-acetonaphthone.

thermostability ($t_{1/2}$ at 40 °C) toward 1-acetonaphthone were measured. Furthermore, a semi-rational design was developed for the three ω-ATAs based on the strategy of selecting key amino acid residues via multiple sequence alignment. The results showed that

these three enzymes simultaneously enhanced activity and thermostability by introducing the amino acid substitutions of G to F, I to A, or L to F, and were consistent with the predicted results (Table 4), indicating that the knowledge obtained from our pocket

Table 4
Specific activity and thermostability of various ATAs and their variants toward 1-acetonaphthone.

Entry	Parent enzyme	Gene ID	The specific activity of parent enzyme (U·g^{-1})[a]	Relative activity	T_m (°C)	The corresponding position of residue				Mutant	The specific activity of mutants (U·g^{-1})	Relative activity of mutants	T_m (°C)
						128	149	182	187				
1	AtATA-Pa	584579684	10.9 ± 0.2	100%	47.6 ± 0.1	R	V	L	L	M4	242.4 ± 2.6	2223.9%	48.4 ± 0.3
2	BCAT	30749295	6.6 ± 1.4	100%	45.1 ± 1.2	G	Y	G	S	G161F (corresponding to L182F)	11.1 ± 1.5	168.2%	47.1 ± 0.3
3	ATA-117-Rd11	914684626	21.9 ± 3.5	100%	48.1 ± 0.7	R	I	F	A	I157A (corresponding to V149A)	33.7 ± 3.0	153.9%	49.5 ± 0.8
4	PdATA	220702511	8.2 ± 1.9	100%	62.8 ± 0.4	—	E	L	E	L56F (corresponding to L182F)	15.1 ± 1.9	184.1%	64.1 ± 0.9

[a] Reaction condition: 10 mmol·L^{-1} amino donor (L-leucine for BCAT, 1-(R)-phenethylamine for ATA-117-Rd11, 1-(S)-phenethylamine for PdATA), 10 mmol·L^{-1} 1-acetonaphthone, 20% (v/v) DMSO, 0.1 mmol·L^{-1} PLP, and 0.25 g·L^{-1} purified enzyme in PBS (50 mmol·L^{-1}, pH 8.0) at 30 °C. Experiments were performed in triplicate.

engineering of AtATA may be significant for engineering ω-ATAs toward 1-acetonaphthone. This further verified that the four key amino acid residues acted as structural switches to control the activity and stability. In addition, ten 1-acetonaphthone analogs were selected to measure the activity, yield, and e.e. value. As shown in Fig. 6, M4 displayed improved activity toward all tested substrates and obtained a high yield and strict e.e. (R > 99.5%) of generated chiral amines compared with AtATA-Pa. These results suggested that M4 exhibits superior performance in catalyzing ketones with different sizes to chiral amines, as well as greater application potential. The detection methods and data refer to HPLC analytical data in Appendix A.
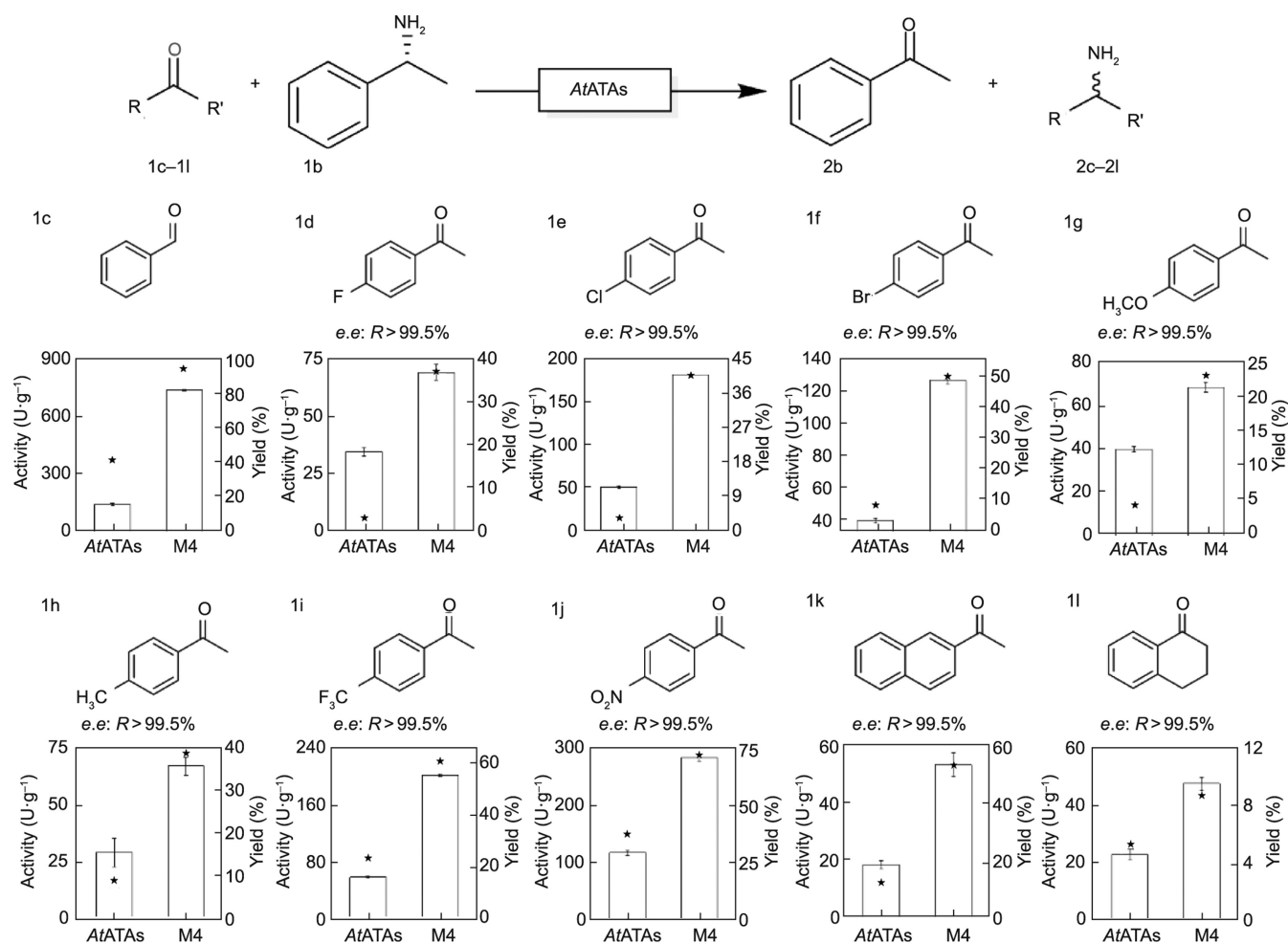

Fig. 6. The relative activity (□) of AtATA-Pa and M4 toward 1-acetonaphthone analogues and the yield (★) of generated products. Reaction conditions: 10 mmol·L^{-1} substrates, 10 mmol·L^{-1} 1-(R)-PEA, 20% (v/v) DMSO, 0.1 mmol·L^{-1} PLP, and 0.02 g·L^{-1} purified enzyme in PBS (50 mmol·L^{-1}, pH 8.0) at 30 °C for activity and chiral selectivity assay. Experiments were conducted in triplicate.

4. Conclusions

In summary, the co-evolution of enzyme activity and thermostability required to acquire robust ATAs is crucial during the synthesis of chiral amines such as (*R*)-NEA. In this study, the key amino acid residues that regulate *At*ATA-Pa activity and stability were identified via engineering of the binding pockets using 1-acetonaphthone as a favorable substrate. Kinetic, sequence, and structural analyses of various *At*ATA-Pa variants provided insights into the molecular mechanisms of substrate-binding and enzyme stability switching. We speculated that the formation of obtuse angles between substrate- and PLP-binding pockets in ATAs and increased π–π interactions between enzymes and substrates were crucial parameters for obtaining ATAs with high activity and thermostability toward 1-acetonaphthone. Based on this hypothesis, we constructed a small and smart mutation library to redesign and recombine four key residues, thereby yielding the "best" mutant (M4), which displayed excellent catalytic activity without sacrificing stability. Using M4 as a biocatalyst, we converted 20 mmol·L^{-1} 1-acetonaphthone into the desired product ((*R*)-NEA) with a yield of 78% yield and *e.e.* (*R* > 99.5%) within 10 h. Moreover, among the ten analogs of 1-acetonaphthone, the yield increased from 3%–50% for *At*ATA-Pa to 9%–100% for M4. Furthermore, we successfully designed and engineered three ATAs that show 8%–22% sequence similarity with *At*ATA via pocket engineering. All three ATAs exhibited synchronously enhanced thermostability and activity. The results of this study demonstrate that the knowledge obtained from protein engineering has the potential to overcome the trade-off between ATA activity and thermostability.

Compliance with ethics guidelines

Jiaren Cao, Fangfang Fan, Changjiang Lyu, Sheng Hu, Weirui Zhao, Jiaqi Mei, Shuai Qiu, Lehe Mei, and Jun Huang declare that they have no conflict of interest or financial conflicts to disclose.

Appendix A. Supplementary material

Supplementary data to this article can be found online at https://doi.org/10.1016/j.eng.2023.04.009.

References

[1] Thorpe TW, Marshall JR, Harawa V, Ruscoe RE, Cuetos A, Finnigan JD, et al. Multifunctional biocatalyst for conjugate reduction and reductive amination. Nature 2022;604(7904):86–91.

[2] Newman DJ, Cragg GM. Natural products as sources of new drugs over the 30 years from 1981 to 2010. J Nat Prod 2012;75(3):311–35.

[3] Zawodny W, Montgomery SL. Evolving new chemistry: biocatalysis for the synthesis of amine-containing pharmaceuticals. Catalysts 2022;12(6):595–616.

[4] Zhang S, Del Pozo J, Romiti F, Mu Y, Torker S, Hoveyda AH. Delayed catalyst function enables direct enantioselective conversion of nitriles to NH$_2$-amines. Science 2019;364(6435):45–51.

[5] Patil MD, Grogan G, Bommarius A, Yun H. Oxidoreductase-catalyzed synthesis of chiral amines. ACS Catal 2018;8(12):10985–1015.

[6] Barniol-Xicota M, Leiva R, Escolano C, Vázquez S. Syntheses of cinacalcet: an enantiopure active pharmaceutical ingredient (API). Synthesis 2016;48(6):783–803.

[7] Yang CY, Li J, Yao YY, Qing C, Shen BC. Enantioseparation of cinacalcet, and its two related compounds by HPLC with self-made chiral stationary phases and chiral mobile phase additives. Curr Pharm Anal 2019;15(2):200–9.

[8] Barman Balfour JA, Scott LJ. Cinacalcet hydrochloride. Drugs 2005;65(2):271–81.

[9] Blaser HU. Enantioselective catalysis in fine chemicals production. Chem Commun 2003;3(3):293–6.

[10] Yasukawa T, Masuda R, Kobayashi S. Development of heterogeneous catalyst systems for the continuous synthesis of chiral amines via asymmetric hydrogenation. Nat Catal 2019;2(12):1088–92.

[11] Ghislieri D, Turner NJ. Biocatalytic approaches to the synthesis of enantiomerically pure chiral amines. Top Catal 2014;57(5):284–300.

[12] Höhne M, Bornscheuer UT. Biocatalytic routes to optically active amines. ChemCatChem 2009;1(1):42–51.

[13] Ghislieri D, Green AP, Pontini M, Willies SC, Rowles I, Frank A, et al. Engineering an enantioselective amine oxidase for the synthesis of pharmaceutical building blocks and alkaloid natural products. J Am Chem Soc 2013;135(29):10863–9.

[14] Batista VF, Galman JL, Pinto GADC, Silva AMS, Turner NJ. Monoamine oxidase: tunable activity for amine resolution and functionalization. ACS Catal 2018;8(12):11889–907.

[15] Völler JS. Metagenomic imine reductases for synthesis. Nat Catal 2021;4(2):2.

[16] Yao P, Marshall JR, Xu Z, Lim J, Charnock SJ, Zhu D, et al. Asymmetric synthesis of N-substituted α-amino esters from α-ketoesters via imine reductase-catalyzed reductive amination. Angew Chem Int Ed Engl 2021;60(16):8717–21.

[17] Xue YP, Cao CH, Zheng YG. Enzymatic asymmetric synthesis of chiral amino acids. Chem Soc Rev 2018;47(4):1516–61.

[18] Wang DH, Chen Q, Yin SN, Ding XW, Zheng YC, Zhang Z, et al. Asymmetric reductive amination of structurally diverse ketones with ammonia using a spectrum-extended amine dehydrogenase. ACS Catal 2021;11(22):14274–83.

[19] Patil MD, Grogan G, Bommarius A, Yun H. Recent advances in ω-transaminase-mediated biocatalysis for the enantioselective synthesis of chiral amines. Catalysts 2018;8(7):254–78.

[20] Yang Q, Zhao F, Zhang N, Liu M, Hu H, Zhang J, et al. Mild dynamic kinetic resolution of amines by coupled visible-light photoredox and enzyme catalysis. Chem Commun 2018;54(100):14065–8.

[21] Rong ZQ, Yu ZY, Weng C, Yang LC, Lu SC, Lan Y, et al. Dynamic kinetic asymmetric amination of alcohols assisted by microwave: stereoconvergent access to tetralin- and indane-derived chiral amines. ACS Catal 2020;10(16):9464–75.

[22] Bhat V, Welin ER, Guo X, Stoltz BM. Advances in stereoconvergent catalysis from 2005 to 2015: transition-metal-mediated stereoablative reactions, dynamic kinetic resolutions, and dynamic kinetic asymmetric transformations. Chem Rev 2017;117(5):4528–61.

[23] Steffen-Munsberg F, Vickers C, Kohls H, Land H, Mallin H, Nobili A, et al. Bioinformatic analysis of a PLP-dependent enzyme superfamily suitable for biocatalytic applications. Biotechnol Adv 2015;33(5):566–604.

[24] Bezsudnova EY, Popov VO, Boyko KM. Structural insight into the substrate specificity of PLP fold type IV transaminases. Appl Microbiol Biotechnol 2020;104(6):2343–57.

[25] Zhai L, Yang S, Lai Y, Meng D, Tian Q, Guan Z, et al. Effect of residue substitution via site-directed mutagenesis on activity and steroselectivity of transaminase *Bp*TA from *Bacillus pumilus* W3 for sitafloxacin hydrate intermediate. Int J Biol Macromol 2019;137:732–40.

[26] Xie DF, Yang JX, Lv CJ, Mei JQ, Wang HP, Hu S, et al. Construction of stabilized (*R*)-selective amine transaminase from *Aspergillus terreus* by consensus mutagenesis. J Biotechnol 2019;293:8–16.

[27] Fesko K, Steiner K, Breinbauer R, Schwab H, Schürmann M, Strohmeier GA. Investigation of one-enzyme systems in the ω-transaminase-catalyzed synthesis of chiral amines. J Mol Catal, B Enzym 2013;96:103–10.

[28] Deepankumar K, Shon M, Nadarajan SP, Shin G, Mathew S, Ayyadurai N, et al. Enhancing thermostability and organic solvent tolerance of ω-transaminase through global incorporation of fluorotyrosine. Adv Synth Catal 2014;356(5):993–8.

[29] Xie YY, Wang JG, Yang L, Wang W, Liu QH, Wang HL, et al. The identification and application of a robust ω-transaminase with high tolerance towards substrates and isopropylamine from a directed soil metagenome. Catal Sci Technol 2022;12(7):2162–75.

[30] Guo F, Berglund P. Transaminase biocatalysis: optimization and application. Green Chem 2017;19(2):333–60.

[31] Siddiqui KS. Defying the activity-stability trade-off in enzymes: taking advantage of entropy to enhance activity and thermostability. Crit Rev Biotechnol 2017;37(3):309–22.

[32] Li SF, Xie JY, Qiu S, Xu SY, Cheng F, Wang YJ, et al. Semirational engineering of an aldo-keto reductase *Km*AKR for overcoming trade-offs between catalytic activity and thermostability. Biotechnol Bioeng 2021;118(11):4441–52.

[33] Cui L, Cui AQ, Li QT, Yang LZ, Liu H, Shao WG, et al. Molecular evolution of an aminotransferase based on substrate-enzyme binding energy analysis for efficient valienamine synthesis. ACS Catal 2022;12(21):13703–14.

[34] Han SW, Park ES, Dong JY, Shin JS. Mechanism-guided engineering of ω-transaminase to accelerate reductive amination of ketones. Adv Synth Catal 2015;357(8):1732–40.

[35] Meng Q, Capra N, Palacio CM, Lanfranchi E, Otzen M, van Schie LZ, et al. Robust ω-transaminases by computational stabilization of the subunit interface. ACS Catal 2020;10(5):2915–28.

[36] Dourado DFAR, Pohle S, Carvalho ATP, Dheeman DS, Caswell JM, Skvortsov T, et al. Rational design of a (*S*)-selective-transaminase for asymmetric synthesis of (1*S*)-1-(1,1′-biphenyl-2-yl)ethanamine. ACS Catal 2016;6(11):7749–59.

[37] Yang L, Zhang K, Xu M, Xie Y, Meng X, Wang H, et al. Mechanism-guided computational design of ω-transaminase by reprograming of high-energy-barrier steps. Angew Chem Int Ed Engl 2022;61(52):e202212555.

[38] Savile CK, Janey JM, Mundorff EC, Moore JC, Tam S, Jarvis WR, et al. Biocatalytic asymmetric synthesis of chiral amines from ketones applied to sitagliptin manufacture. Science 2010;329(5989):305–9.

[39] Novick SJ, Dellas N, Garcia R, Ching C, Bautista A, Homan D, et al. Engineering an amine transaminase for the efficient production of a chiral sacubitril precursor. ACS Catal 2021;11(6):3762–70.

[40] Łyskowski A, Gruber C, Steinkellner G, Schürmann M, Schwab H, Gruber K, et al. Crystal structure of an (R)-selective ω-transaminase from *Aspergillus terreus*. PLoS One 2014;9(1):e87350.

[41] Huang J, Xie DF, Feng Y. Engineering thermostable (R)-selective amine transaminase from *Aspergillus terreus* through in silico design employing B-factor and folding free energy calculations. Biochem Biophys Res Commun 2017;483(1):397–402.

[42] Cao JR, Fan FF, Lv CJ, Wang HP, Li Y, Hu S, et al. Improving the thermostability and activity of transaminase from *Aspergillus terreus* by charge-charge interaction. Front Chem 2021;9:664156.

[43] Baud D, Ladkau N, Moody TS, Ward JM, Hailes HC. A rapid, sensitive colorimetric assay for the high-throughput screening of transaminases in liquid or solid-phase. Chem Commun 2015;51(97):17225–8.

[44] Niesen FH, Berglund H, Vedadi M. The use of differential scanning fluorimetry to detect ligand interactions that promote protein stability. Nat Protoc 2007;2 (9):2212–21.

[45] Purmonen M, Valjakka J, Takkinen K, Laitinen T, Rouvinen J. Molecular dynamics studies on the thermostability of family 11 xylanases. Protein Eng Des Sel 2007;20(11):551–9.

[46] Yuan SG, Chan HCS, Hu ZQ. Using PyMOL as a platform for computational drug design. WIREs Comput Mol Sci 2017;7(2):e1298.

[47] Parvez A, Ravikumar Y, Bisht R, Yun J, Wang Y, Chandrika SP, et al. Functional and structural roles of the dimer interface in the activity and stability of *Clostridium butyricum* 1,3-propanediol oxidoreductase. ACS Synth Biol 2022;11 (3):1261–71.

[48] Yu X, Wang X, Engel PC. The specificity and kinetic mechanism of branched-chain amino acid aminotransferase from *Escherichia coli* studied with a new improved coupled assay procedure and the enzyme's potential for biocatalysis. FEBS J 2014;281(1):391–400.